EXAFS Measurements of Laser-Generated Shocks with an Imploded Target as a Radiation Source

Introduction

Recently, great interest has been shown in the study of dynamic material response to shocks of high pressure and high strain rate.[1,2] Shocks of up to ~1 Mbar and strain rates of $\sim 10^7$ to 10^8 s^{-1} were generated in metals (Al, Cu) by laser irradiation. The laser intensity in those experiments ($\sim 10^{11}$ W/cm^2) was high enough to raise the pressure above the Hugoniot elastic limit (HEL) but low enough for the compressed material to remain solid. Using Bragg and Laue x-ray diffraction, the experiments clearly showed the retention of crystallinity during the passage of the shock. Silicon under these conditions was found to compress elastically, i.e., only in the direction of shock compression. Copper, on the other hand, was found to compress equally in all dimensions, indicating the transition to plastic flow. These differences were explained in terms of the different velocity of dislocation propagation that gives rise to the elastic–plastic transition.

The goal of this work is to examine the use of EXAFS[3] (extended x-ray absorption fine structure) as a complementary characterization of such laser-shocked metals. EXAFS modulations above an absorption edge are due to the interference of the ejected photoelectron wave with the reflected wave from neighboring atoms. Thus, the interference translates into modulations in the cross section for photon absorption above the edge. The frequency of these modulations relates to the inter-particle distance, hence the density of the compressed material. The decay rate of the modulation with increasing photoelectron energy yields the MSRD (mean-square relative displacement) and can thus serve as a temperature diagnostic. EXAFS had originally been applied to crystalline materials but has since been widely used to study amorphous,[4–6] liquid,[7–9] heated,[8,10–17] or compressed[11,14–16,18,19] materials. In those steady-state experiments, the imposed temperature is known independently and the main emphasis is on studying the chemical structure. In this experiment the emphasis is on measuring the compression and temperature of the shocked material through the EXAFS spectrum itself. There is an important difference between the diffraction experiments and the present EXAFS experiment: EXAFS, which depends only on short-range order, does not require the use of single-crystal samples, as was the case in the diffraction experiments. In this experiment we use polycrystalline Ti foils in which the number of crystalline grains under the laser focal spot is very large. Thus, the shock direction is randomly distributed with respect to the atomic planes. It is known that the same stress can cause elastic or plastic deformation in the same crystal, depending on the orientation of the shock direction with respect to the crystal planes.[20] Since the transition to plastic flow depends on the propagation of dislocations along slip planes, we can expect a plastic response in some or most of the crystalline grains. Like in the shock experiments in silicon and copper cited above,[1,2] the shock pressure in our experiments (~0.4 Mbar) is much higher than the Ti HEL.[21] *The assumption of three-dimensional compression, required to relate the EXAFS-determined inter-atomic distance to the density, can be tested by comparison with the measurement of shock speed, which yields the compression (through the known Hugoniot).*

Most EXAFS experiments are performed with a synchrotron radiation source, and the spectrum due to a sample in steady state is slowly scanned. In laser experiments[22–24] the entire spectrum is recorded simultaneously during the short pulse (~ns) of the laser. This makes it challenging to obtain an EXAFS spectrum of high signal-to-noise ratio. In a previous paper[25] we have shown that a CH shell imploded by a multibeam laser system constitutes a source of an intense and smooth spectrum of x-ray radiation, suitable for EXAFS measurements. The high source intensity enables us to work with a thick Ti foil (attenuation $\sim e^{-3}$ above the K edge), which increases the relative modulations in the observed signal. Using the 60-beam OMEGA laser,[26] the intensity from imploded shells around 5 keV was sufficient to obtain a good EXAFS spectrum above the K edge of Ti at 4.96 keV. Fitting a theoretical model to the measured EXAFS spectrum yielded the inter-particle distance and temperature in agreement with synchrotron results.[27,28] Those absorption experiments were performed on cold, unshocked Ti foils in order to test the reliability of the present method, which is here extended to the shocked case.

Titanium was chosen because of the following considerations: The EXAFS spectrum from a low-Z absorber, because of the high attenuation in our experiment, would be dominated by the second-order crystal diffraction (whose attenuation is much smaller). In Ti the second-order radiation (around ~10 keV) is too weak to affect the results. On the other hand, for a higher-Z absorber the imploding-target emission at the corresponding higher photon energy would be too weak. Titanium behavior is complicated, however, by phase transitions:[29] at normal conditions Ti crystallizes as hexagonal close packed (α-Ti); as the pressure rises, it transforms to a hexagonal phase (ω-Ti) at low temperatures, or to a body-centered cubic (β-Ti) at high temperatures. For shocked titanium a transition from α-Ti to ω-Ti has been shown[30] to occur at a pressure of ~0.12 Mbar; this value varies with the sample purity but it is clearly much lower than the pressure in this experiment (~0.4 Mbar). Following this transition there may be an additional transition of ω-Ti to β-Ti, but the Hugoniot shows no additional discontinuity up to ~1.2 Mbar[31] and static-pressure studies showed no such transition for pressures as high as 0.87 Mbar.[32] Recently, a new Ti phase (γ) has been discovered[33] but it is reached at a higher pressure (~1.1 Mbar) than relevant to this experiment. We next address the question of the time constant t_0 for the (α-Ti) to (ω-Ti) phase transition. Although previous phase transitions in Ti have been observed with much lower strain-rate shocks, a pressure dependence of t_0 has been determined[34] that can be extrapolated to the pressure (~0.4 Mbar) in this experiment. In the range of 0.05 to 0.09 Mbar, the time constant decreases exponentially with the pressure; extrapolating to $P = 0.4$ Mbar yields $t_0 \ll 1$ ns. The phase transition α-Ti to ω-Ti entails a 1.9% decrease in volume,[33] much smaller than the implied volume change due to the compression. However, the change in crystal structure strongly affects the EXAFS spectrum as the geometry of the nearest neighbors is now more complex.[35]

The theory of EXAFS[3] yields an expression for the normalized modulations $\chi(k) = \mu(k)/\mu_0(k) - 1$, where $\mu(k)$ is the absorption coefficient (or opacity) and $\mu_0(k)$ is the absorption of the isolated atom (i.e., without the EXAFS oscillations). $\mu_0(k)$ can be obtained by passing a smooth curve through the EXAFS oscillations. k is the wave number of the ejected photoelectron and is given by the de Broglie relation $\hbar^2 k^2/2m = E - E_K$, where E is the absorbed photon energy and E_K is the energy of the K edge. For low disorders and polycrystalline materials, the basic EXAFS theory,[3] assuming single-electron scattering and plane electron waves and neglecting multiple scattering, yields the following expression for the normalized modulations $\chi(k)$:

$$\chi(k) = \sum_j N_j S_0^2 F_j(k) \exp\left[-2\sigma^2 k^2 - 2R_j/\lambda(k)\right] \times \sin\left[2kR_j + \phi_j(k)\right]/kR_j^2, \quad (1)$$

where N_j is the number of atoms surrounding the absorbing atom at a distance R ($N_1 = 12$ in Ti). The sum over j relates to successive shells of atoms around the photo-absorbing atom. Only the first coordination shell will be of interest here because it suffices for determining the density; also, in the shocked material the contribution of higher shells essentially disappears. R is the interparticle distance, and the factor σ^2 (Debye–Waller factor) accounts for thermal vibrations, derived from a harmonic potential. σ^2 can also include static disorder $\left(\sigma^2_{\text{total}} = \sigma^2_{\text{vibration}} + \sigma^2_{\text{disorder}}\right)$, corresponding to a Gaussian distribution of pair distances. The backscattering amplitude $F(k)$ and phase-shift factor $\phi(k)$ for titanium were calculated by Teo and Lee.[36] McKale *et al.*[37] have improved these calculations by removing the assumption of photoelectron plane waves; their results differ from those of Teo and Lee, primarily for $k \leq 3$. We have averaged the results of McKale *et al.* for scandium and vanadium (their calculations apply to every other element) and have made a minor adjustment to fit the Ti results of Teo and Lee at high wave numbers. The mean free path of the ejected electron for inelastic collisions in titanium, $\lambda(k)$, was taken from Blanche *et al.*[27] The vibration amplitude σ^2 and the interatomic distance R are treated as adjustable parameters in fitting Eq. (1) to the experimental EXAFS spectrum. In addition, the adjustable constant $S_0^2 (< 1)$ accounts for multi-electron effects such as relaxation of the core hole and excitation of other than the ejected photoelectron.[3] Finally, an adjustable energy shift ΔE is applied to the experimental points to account for uncertainties in chemical-bonding and core-relaxation effects. The edge energy ($k = 0$) is initially determined by the inflection point, i.e., the energy for which the derivative of the falling intensity above the edge is maximal. The distance R can yield the density of the absorber. The temperature can be found from the σ^2 value, which depends also on the density. Beni and Platzman[38] have calculated σ^2 as a function of temperature using the Debye model for the phonon density of states, including correlation between the motions of the central and neighboring atoms. We use the first term in their result (including a factor-of-2 correction[10]), neglecting the correlation term. Greegor and Lytle[10] have compared the results of Beni and Platzman[38] to their measurements (in copper) and have shown that neglecting the correlation term increases σ^2 by about 20%. We therefore reduced the uncorrelated results for Ti by 20%. As a check, we compared

the measured values[7] of σ^2 for Zn in the temperature range of 0.01 to 0.06 eV with those calculated by the procedure described here, and they agree to within a few percent. σ^2 depends on the density through the Debye temperature. Using an empirical model[39] we calculate the density dependence of the Debye temperature (in eV) as

$$\Theta_B = -14.79 + 50.39\left(\rho/\rho_s\right) + \left(\rho/\rho_s\right)^2, \qquad (2)$$

where ρ is the density and ρ_s is the solid density. We show in Fig. 94.38 the calculated σ^2 for Ti as a function of temperature and density. As seen, compression increases the amplitude of the EXAFS signal because of the decrease in σ^2. This is in addition to the increase because of the explicit $1/R^2$ dependence in Eq. (1). On the other hand, compression reduces the EXAFS signal because $\lambda(k)$ in Eq. (1) depends on the density ρ as $1/\rho$.

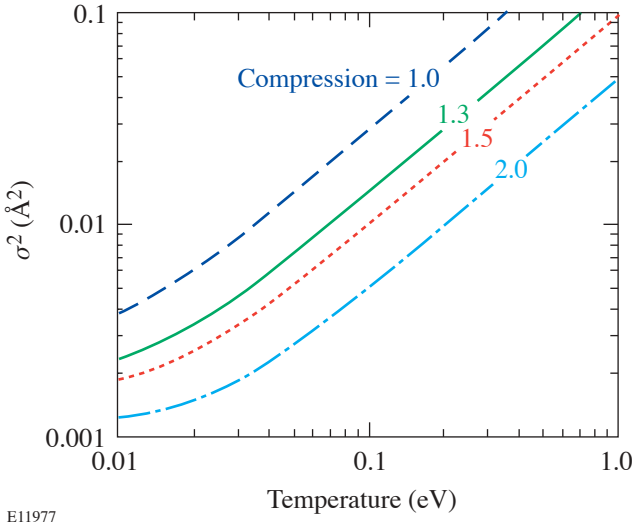

Figure 94.38
Calculated σ^2 due to thermal vibrations for Ti from the model of Beni and Platzman[38] making use of the density dependence of the Debye temperature from Ref. 39. Correlation was accounted for by reducing the first, uncorrelated term in Ref. 38 by 20%.

Although advanced EXAFS models have been developed,[40–42] the use of Eq. (1) is adequate for our experiments: curved-wave effects are included in the calculations[37] of phase shift and backscattering amplitude, multi-electron effects are accounted for by the S_0^2 factor, and multiple scattering is negligible for the first coordination shell,[43] the only one of interest here.

Experiment

Figure 94.39 shows a schematic view of the target used to measure EXAFS spectrum in laser-shocked targets. Fifty-seven beams of the OMEGA laser, of ~21-kJ total energy, are focused on an empty CH shell whose implosion generates the radiation source for measuring the absorption spectrum in Ti. The three remaining OMEGA beams are stacked and used to irradiate and launch a shock wave in Ti. The laser pulse shape was 1 ns square; thus the three stacked beams formed a 3-ns-long square pulse; these beams were focused onto the plane target in a 3.8-mm-diam focal spot, giving an irradiance of 0.5 TW/cm^2. A delay time for the three stacked beams with respect to the rest of the beams was adjusted so that peak implosion of the spherical target occurred when the shock had just traversed the Ti layer. The spherical target had a diameter ~940 μm and a thickness ~20 μm. The planar target consisted of 10-μm-thick polycrystalline Ti, coated on both sides with 17 μm of CH. The purpose of the front CH layer was to prevent laser heating and ablation of the Ti. The purpose of the back CH layer was to prevent the shock unloading at the back Ti surface. The thickness of the Ti layer d was the highest ($\mu_0 d \sim 3$) that still yielded significant x-ray signal after K-edge absorption. A thicker absorber yields higher EXAFS modulations in the observed intensity I since $(\Delta I/I) \sim (\mu_0 d)(\Delta\mu_0/\mu_0)$. From the point of view of signal-to-noise (S/N) ratio, the optimal value of $\mu_0 d$ depends on the source of noise: for photon noise ($\sim I^{1/2}$) it can be shown to be 2. When the noise is proportional to I, the S/N ratio continuously increases with $\mu_0 d$. We found the latter to be the case here. The CH thickness and laser pulse length were chosen to minimize nonuniformity in the Ti properties in the direction of the shock (see Fig. 94.43 later in article).

The heat shield (0.5-mm-thick CH foil) minimizes the heating of the Ti layer due to radiation from the imploding spherical target. It attenuates the EXAFS-producing radiation at ~5 keV by a factor of ~2.5 while very strongly attenuating the softer radiation, which can heat the Ti foil. The functioning of the heat shield was tested (see below) by measuring the EXAFS spectrum when the three shock-launching beams were not fired.

Two x-ray spectrometers measured the spectrum on calibrated film.[44] One x-ray spectrometer (XRS-I) measured the EXAFS spectrum, the other (XRS-II) the incident spectrum I_0. A typical I_0 spectrum is shown in Fig. 2(a) of Ref. 25. To cross-calibrate the two spectrometers, a 10-μm-thick Ti foil was placed on some shots in front of XRS-II, and its EXAFS spectrum was compared with that obtained in XRS-I without launching a shock. The spectral resolution of the spectrometer

is limited by the source size. The FWHM size of the core seen at 5 keV (Fig. 1 in Ref. 25) is $D \sim 100\ \mu$m; this translates to a spectral resolution $\Delta E = ED/tg(\Theta_B)L$, where L is the distance from the target to the film and Θ_B is the Bragg angle. This yields a resolution of ~5 eV, much smaller than a typical EXAFS modulation period (~60 eV).

Although the EXAFS measurement is time integrated, a meaningful shock diagnosis can be obtained without streaking the spectrum in time because the x-ray pulse width is very short. We previously showed[25] that the emission from the spherical target above the Ti K edge (~5 keV) comes mostly from the compressed core, whereas the emission from the laser-absorption region is much weaker. This was seen in both the time-resolved spectrum as well as the space-resolved spectrum. The former showed that the pulse width of the x-ray emission at ~5 keV was only ~120 ps [Fig. 2(b) in Ref. 25], much shorter than the shock transit time through the Ti (~2 ns).

The implosion of the spherical target has to be timed so as to probe the Ti layer after it is traversed by the shock. This is because the EXAFS spectrum of a partly shocked foil is dominated by the low-temperature region ahead of the shock front. The delay of the shock-launching beam with respect to the implosion beams is given by the difference τ(implosion) – τ (Ti), where t (implosion) is the compression time of the spherical target and τ(Ti) is the shock arrival time at the back of the Ti layer. Both these times have been measured; they are also known from simulations by the hydrodynamic code *LASNEX*.[45] The implosion time is determined by streaking the soft-x-ray emission from the spherical target. Since the emission above the Ti K edge (~5 keV) is completely dominated by the compressed core, in order to see the coronal emission during the rising part of the laser, we streak the spectrum at the softer energy of ~3 keV (see Fig. 94.40), where the compressed-core emission is completely saturated. The indicated compression time is ~1.7 ns.

The time τ(Ti) is determined experimentally by the method of active shock breakout (ASBO).[46] Figure 94.41 shows the corresponding experimental configuration and a sample result. An EXAFS target (Fig. 94.39) was irradiated at the same intensity as in the EXAFS experiment. A frequency-tripled YAG laser, synchronized with OMEGA, irradiated the backside of the target and interfered with the reflected beam. Figure 94.41 shows the interference fringes measured by a streak camera, viewing the central portion of the focal spot. Also shown is a series of simultaneously recorded fiducial time pulses marking the time scale; the time $t = 0$ corresponds to the start of the laser pulse. Initially, the laser is reflected from the backside of the Ti foil. When the shock reaches this surface [at time τ(Ti)], the reflection is seen to be disrupted. This is the

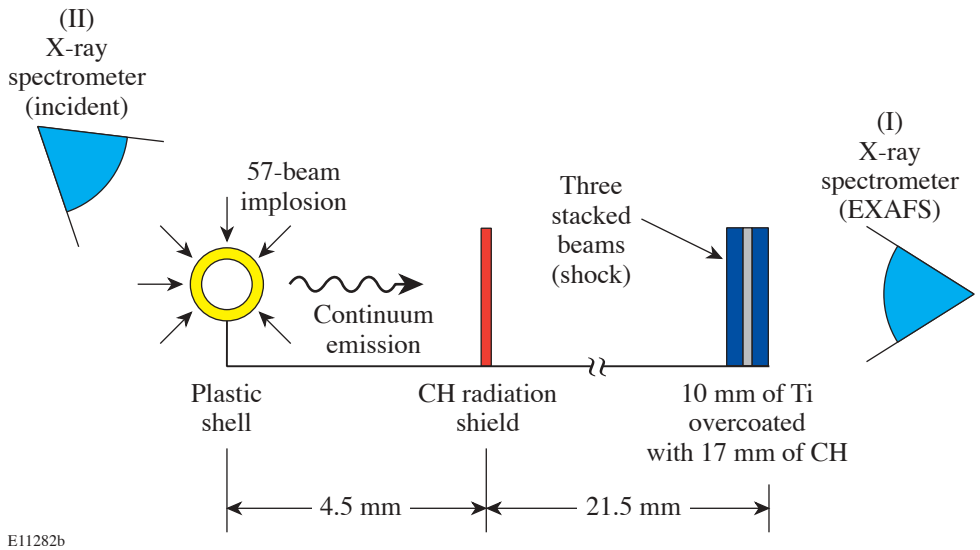

Figure 94.39
Schematic view of the target. The imploding spherical target serves as a radiation source for EXAFS measurements. X-ray spectrometer I measures the EXAFS spectrum; x-ray spectrometer II measures the incident spectrum I_0. The heat shield minimizes the heating of the shocked Ti layer due to radiation from the imploding spherical target.

optimal time for EXAFS probing. Subsequent to this, a weaker reflection from the backside of the CH layer is seen; when the shock reaches that surface, at time τ(CH), ablation sets in, the laser is strongly absorbed, and reflection disappears. It is not mandatory to know τ (Ti) with great precision in setting the delay between the shock-launching beam and the backlighter beams. This is because we repeat the experiment for different time delays around the expected optimal value; when the shock arrives at the back surface of the Ti layer, the EXAFS spectrum clearly changes into a lower-intensity, faster-decaying spectrum.

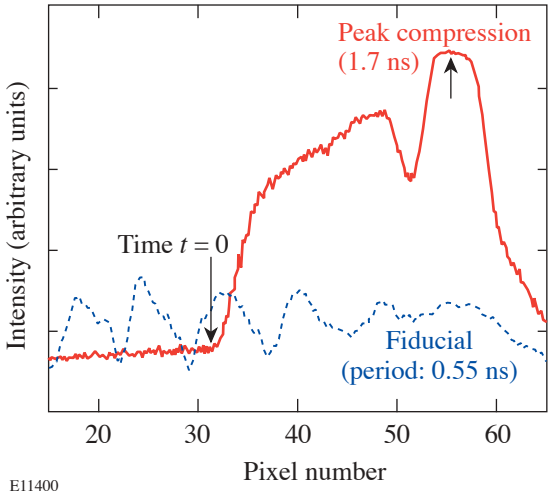

Figure 94.40
Streaked x-ray spectral intensity around ~3 keV emitted by the imploding spherical shell. The streak is used to determine the implosion time, which is required for determining the EXAFS probing time.

The ASBO data can also be used to determine the shock velocity, i.e., the shock strength. Since the time τ(Ti) includes the time of shock travel through the front CH layer, we can use the difference τ(CH) – τ(Ti) to find the net transit time through the Ti layer. For that we assume that the travel time through the two CH layers is the same. This was verified by code simulations to be correct to within a few percent. For an irradiance of 0.5 TW/cm^2 (the case analyzed by EXAFS below) the shock velocity in the Ti layer was found to be ~6.3 km/s, which, according to the Ti Hugoniot,[31,47] corresponds to a pressure of 0.4 Mbar and compression of 1.28. *An agreement of the density as measured by EXAFS and the density derived from the shock speed through the Hugoniot (as is the case below) is a confirmation of the assumption of 3-D compression.*

Finally, the ASBO data show the velocity nonuniformity across the shock front to be ±10%, which, according to the Hugoniot of Ti, translates into a nonuniformity of ±4% in the pressure as well as in the density. *LASNEX* runs show that the

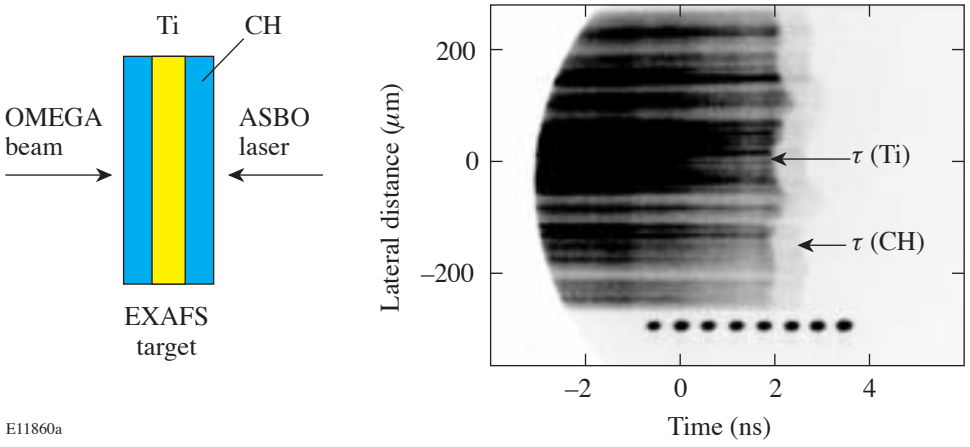

Figure 94.41
Active shock breakout (ASBO) measurement of the arrival time τ (Ti) of the laser-launched shock at the back surface of the Ti layer. Time t = 0 corresponds to the start of the laser pulse. This measurement is also used to assess the shock nonuniformity and to confirm (through the Hugoniot) the EXAFS-measured compression.

average density variation during the probing time interval (~120 ps) is less than 2%, as is the density variation along the shock direction (Fig. 94.43). These uncertainties are much smaller than the change in density due to the compression, as shown below.

Hydrodynamic Simulations

To determine the expected shock strength and the properties of the shocked Ti for a given laser irradiation, the hydrodynamic code *LASNEX* was used for one-dimensional simulations. It includes the "quotidian" equation of state[39] (QEOS), based on the Thomas–Fermi equation of state with empirical corrections. As an indication of its validity at low temperatures we compare in Fig. 94.42 curves of QEOS pressures at constant Ti compression with experimental points[33] obtained recently for Ti in a diamond anvil cell at room temperature and the same compressions. The agreement is quite good; however, the curves also show the low sensitivity to the temperature, which reduces the precision in the temperature prediction.

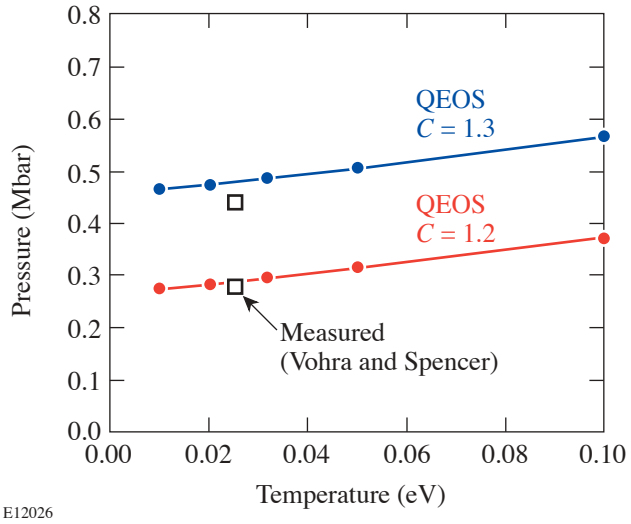

Figure 94.42
QEOS curves for two compression values in Ti. Experimental values obtained in a diamond anvil cell at room temperature for the same compression values are also shown.[33]

The *LASNEX*-calculated profiles of density, pressure, and temperature for a laser irradiance of 0.5 TW/cm^2 are shown in Fig. 94.43 at the time of arrival of the shock at the rear surface of the Ti layer, namely 3.5 ns. These simulations correspond to the experimental results discussed below. The profiles, particularly that of the density, are seen to be quite uniform throughout the Ti. The average value of density within the Ti (~5.6 g/cm^2) and the average value of pressure (~0.4 Mbar) are consistent with the measured[31,47] Hugoniot of Ti. As will be shown in the next section, the measured EXAFS spectrum at about the time 3.5 ns yields a compression of 1.3 (assuming three-dimensional compression), as compared with a compression of 1.25 in these simulations. Code runs with an initial temperature higher than room temperature showed that the temperature due to radiation preheat can simply be added to the calculated temperature profiles.

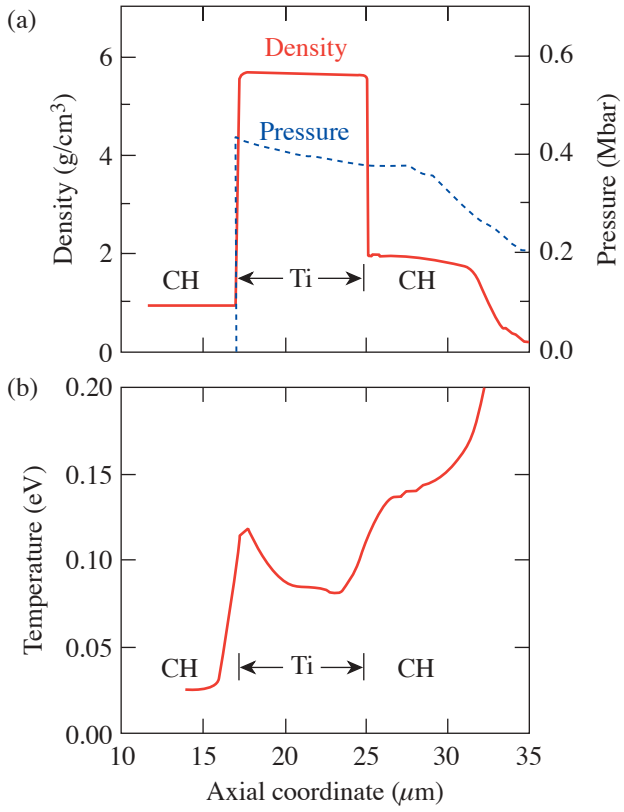

Figure 94.43
LASNEX-calculated profiles of (a) density and pressure and (b) temperature for a laser irradiance of 0.5 TW/cm^2 at the time of arrival of the shock at the back surface of the Ti layer, namely 3.5 ns. The laser is incident from the right.

Results and Analysis

1. Radiation Heating

The extraction of the experimental $\chi(k)$ to be compared with Eq. (1) follows the standard procedure.[3] First, the absorption coefficient $\mu = \log(I_0/I)$ is computed from the measured intensities. As explained before, no correction for the finite spectral resolution (~5 eV) was required. Likewise, higher-harmonic contribution to the crystal diffraction could be ignored: the spectrum emitted by the implosion had a characteristic temperature ~1 keV; thus the second-order radiation at 10 keV

was weaker than the first order by a factor of $\sim e^5$, in addition to its lower crystal reflectivity. The normalized EXAFS spectrum $\chi(k)$ was calculated using the McMaster adjustment:[48]

$$\chi(k) = \left\{\left[\mu(k) - \mu_0(k)\right]/\Delta\mu\right\}\left[\Delta\mu^{\text{th}}(k=0)/\Delta\mu^{\text{th}}(k)\right], \quad (3)$$

where $\Delta\mu$ is the measured jump at the K edge and $\Delta\mu^{\text{th}}(k)$ is the theoretical net K-shell absorption.

To study the effect of shocks on the Ti metal, the effect of radiation heating should be minimal. This was verified by measuring the EXAFS spectrum with the target of Fig. 94.39 but without launching a shock. Figure 94.44 shows the measured normalized EXAFS spectrum $\chi(k)$ for such a shot. Next, the $\chi(k)$ due to the first coordination shell is extracted as explained in Ref. 25: $k\chi(k)$ is Fourier transformed to the real space and the first peak is filtered and transformed back to the k space. We use $k\chi(k)$ to de-emphasize the low-k region, where the theory is imprecise. We next fit Eq. (1) to the filtered spectrum while varying R, σ^2, S_0^2, and ΔE_0. Figure 94.45 shows the best fit. Before performing the fit, the theoretical profile was subjected to the same Fourier filtering as the experimental spectrum (in particular, using the same k range); this increases the quality of the fit. The best fit was obtained with $R = 2.93$ Å, $\sigma^2 = 0.011$ Å^2, $S_0^2 = 0.86$, and $\Delta E = 13$ eV. The value of σ^2 corresponds according to Fig. 94.38 to $T =$ 40 meV. Thus the radiation heating above room temperature amounts to only ~15 meV. As shown below, this is much smaller than the shock heating. Since the incident x-ray intensity in successive shots is not entirely reproducible, we normalize the heating in each shot by the corresponding intensity of x-ray emission at 5 keV. The explanation of the fitting and the calculation of the error bars are explained in the Appendix.

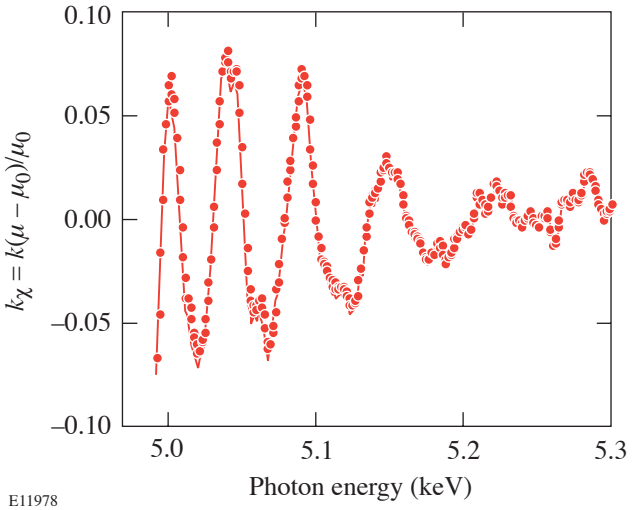

Figure 94.44
Normalized EXAFS spectrum $\chi(k)$ before Fourier filtering for an unshocked shot, used to determine the temperature rise due to radiation heating.

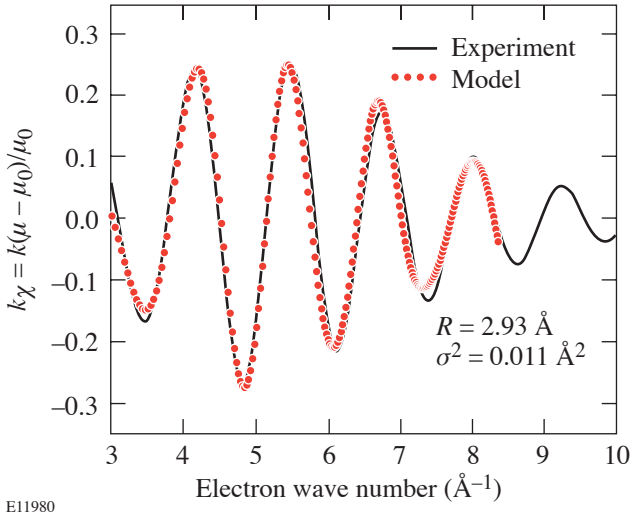

Figure 94.45
Fitting of the model [Eq. (1)] to the observed $k\chi(k)$ EXAFS spectrum from Fig. 94.42. The parameter values (R and σ^2) giving the best fit are shown. The value of R agrees with the known value for Ti at normal conditions. σ^2 corresponds to a temperature of ~40 meV.

2. Shock Compression

Shock-compression experiments using the 3-ns, 0.5-TW/cm^2 laser irradiation have been performed by varying the shock probing time, given by the delay between the shock-launching beams and the compression beams. The appropriate shock probing time for a 3-ns laser pulse, an irradiation of 0.5 TW/cm^2, and the target described above was found to be ~3.5 ns, both through ASBO measurements and *LASNEX* code simulations. In successive shots we probed the shocked Ti both before and after that time. At around a probing time of ~3.5 ns the EXAFS clearly changed to a faster-decaying spectrum: the number of clearly visible modulations dropped from ~6 to ~3. The results at a probing time ~3.5 ns indeed show a compression of the Ti layer. To illustrate the compression directly we compare in Fig. 94.46 the measured absorption spectra (before Fourier filtering) for two probing times: before the shock enters the Ti layer (marked "before shock arrival") and when the shock has just traversed the Ti layer (marked "after shock arrival"). The lengthening of the EXAFS period of modulation in the after-shock case is evidence of compression. The two shots were identical except for the different delay time. The

curve marked before shock is shifted by 5 eV toward higher wave numbers for a clearer demonstration of the lengthening. The effect of the shock is also seen in increasing the damping rate of the modulations. Figure 94.47 shows the fitting of Eq. (1) to the Fourier-filtered experimental spectrum. The value of R for the best fit is (2.68±0.05) Å, which is smaller by a factor of ~1.1 than the value R = 2.92 Å for an unperturbed Ti. The difference between the two values is much larger than the uncertainty in R. Assuming the compression is three-dimensional, this corresponds to a volume compression by a factor of ~1.3 or a density of 5.8 g/cm^3. This agrees with the compression value derived above from the measured shock velocity (1.28) as well as with the average compression (1.25) of the profile calculated by *LASNEX* (Fig. 94.43). This agreement supports the assumption of three-dimensionality, which was also postulated above, based on the fact that a polycrystalline Ti sample was used in this experiment.

The value of σ^2 (namely, 0.033) is much higher than in the unshocked case (Fig. 94.45). According to Fig. 94.38, this value would correspond to a temperature of ~0.24 eV, much higher than the value ~0.09 predicted by *LASNEX* (Fig. 94.43). We conclude that σ^2 has a contribution from static disorder in addition to thermal vibrations, due possibly to the α-Ti to ω-Ti phase transformation. A large σ^2 value has also been found in EXAFS measurements applied to various disordered systems.[5,6,15,17] In particular, it has been shown[15] that a Ge crystal transformation from diamond type to white-tin type at 0.11 Mbar is accompanied by a quadrupling in the value of σ^2. Similarly, a doubling in the value of σ^2 was found[17] to accompany the order–disorder transition in CuI; finally, we cite measurements[16] on compressed Ga close to room temperature where, because of phase transformation, values of σ^2 comparable to the result of Fig. 94.47 have been measured. It should be emphasized that the increase in σ^2 cannot be due to melting. First, the melting temperature of Ti at normal conditions is ~0.17 eV, but at a compression of 1.3 it rises to ~0.3 eV as calculated by the Lindemann law,[49] thus certainly higher than the temperature in the shocked Ti. Moreover, experiments have shown that melting does not cause an increase in σ^2 beyond that associated with the increase in temperature.[9]

In the initial α-Ti crystal each atom is surrounded by 12 atoms at a distance of 2.92 Å. In the more-complex ω-Ti geometry[35] the arrangement of neighboring atoms is of two kinds, described as site A and site B. For every atom in site A there are two atoms in site B. Site-A atoms have 14 nearest neighbors at a distance of 2.92 Å. Site-B atoms have three

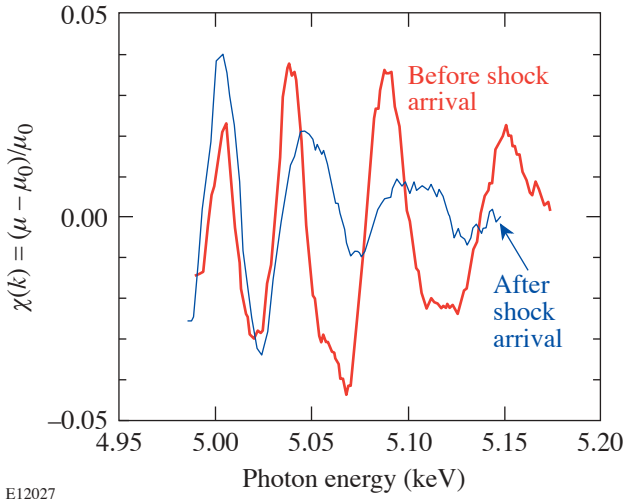

Figure 94.46
Demonstration of shock compression based on the lengthening of the EXAFS period of modulation. The two normalized EXAFS spectra (shown before Fourier filtering) correspond to different probing times from otherwise identical shots. The curve marked "after shock arrival" corresponds to the time when the shock has just traversed the Ti layer. The curve marked "before shock arrival" corresponds to a time before the shock entered the Ti layer.

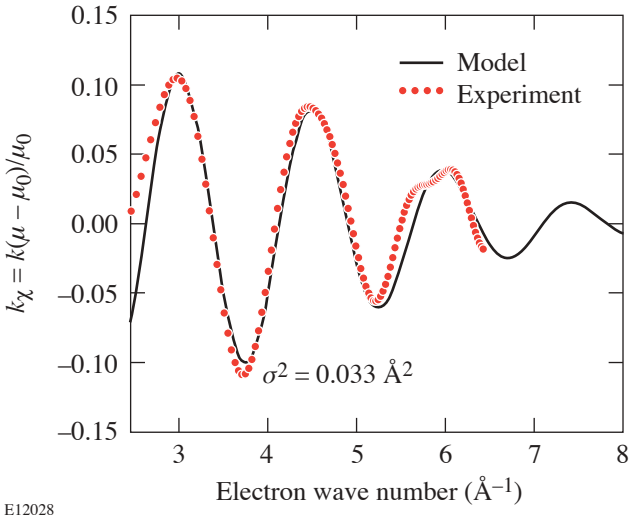

Figure 94.47
Fitting of the model [Eq. (1)] to the observed $k\chi(k)$ EXAFS spectrum (derived from the curve labeled "after shock arrival" in Fig. 94.44, after Fourier filtering). The parameter values giving the best fit are shown. The interatomic distance R yields a compression of 1.3 (assuming to be three-dimensional) and the factor $\sigma^2 = \sigma^2_{\text{therm}} + \sigma^2_{\text{stat}}$ contains both the temperature-dependent vibrations term and a static disorder term.

neighbors at a distance of 2.667 Å, six neighbors at a distance of 2.845 Å, and two atoms at a distance of 3.023 Å. Thus, there is a spread of ~0.3 Å (or ~10%) in the first-shell distances. This has the effect of adding a disorder term to the thermal disorder due to crystal vibration. The different distances translate to EXAFS modulation of different frequencies. The beating of these frequencies when calculating the total EXAFS spectrum gives rise to a decreasing amplitude. Thus, EXAFS spectra can be used to study *dynamic* α-Ti to ω-Ti phase transformation in shock compression. On the other hand, to reliably extract the temperature value from the EXAFS spectrum, a metal that does not undergo a phase transformation should be used. For example, in vanadium no phase transformation has been found up to pressures of 1 Mbar.[29] A smaller σ^2 value in a comparable shocked vanadium experiment would support the conclusion that a phase transformation in the titanium experiment has actually taken place.

To assess the observability of EXAFS in future titanium experiments we plot in Fig. 94.48 the contours of $\max(|\chi|)$ in the compression-temperature space. We divide the contour-value scale into three regions: (a) $\max(|\chi|) > 0.05$, termed high; (b) $0.03 < \max(|\chi|) < 0.05$, termed marginal; and (c) $\max(|\chi|) < 0.03$, termed low. EXAFS can readily be measured in the first region and only marginally in the second [for solid titanium at room temperature $\max(|\chi|) \sim 0.06$]. To show what part of the compression-temperature space can be accessed by shocks we superimpose on the contours in Fig. 94.48 the values along the principal Hugoniot of Ti.[31,47] As seen, strong shocks are not readily measurable with EXAFS. On the other hand, isentropic (low-temperature) compressions of metals are much more suitable for EXAFS measurements. Figure 94.48 also shows the calculated isentrope that passes through the Hugoniot point corresponding to the present experiment (Fig. 94.47). It was obtained by using the Cowan model for the density dependence of the Gruneisen (γ) of Ti,[39] normalized to the experimental value (~1.17) at solid density.[30] Obviously, even a near-isentropic compression will be much easier to diagnose with EXAFS than a shock of comparable compression.

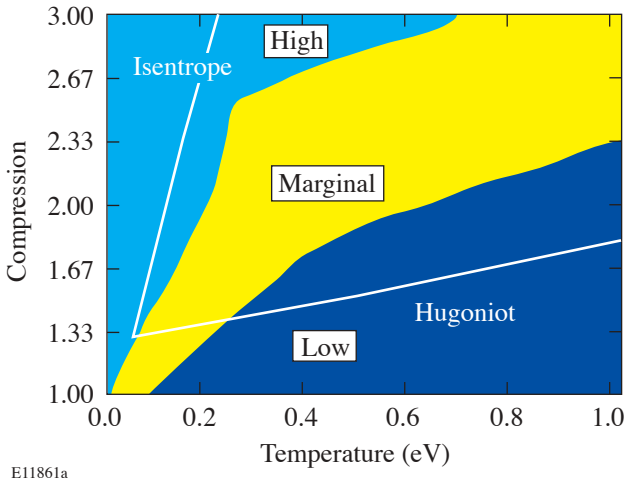

Figure 94.48
Regions of observability of EXAFS in compressed titanium. High: $\max(|\chi|) > 0.05$; marginal: $0.03 < \max(|\chi|) < 0.05$; and low: $\max(|\chi|) < 0.03$. The Hugoniot for Ti[31,46] is shown as well as the isentrope, both passing through the point corresponding to the present experiment.

Further understanding of high-strain-rate shock compression of metals can be gained in future experiments by (a) performing similar experiments on single-crystal samples and comparing EXAFS and multidirectional diffraction measurements, (b) employing a target material that does not undergo phase transformation below ~1-Mbar pressure (e.g., vanadium[29]), and (c) performing near-isentropic compression experiments where higher densities at lower temperatures can be achieved.

ACKNOWLEDGMENT

This work was supported by the U.S. Department of Energy Office of Inertial Confinement Fusion under Cooperative Agreement No. DE-FC03-92SF1931,460, the University of Rochester, and the New York State Energy Research and Development Authority. The support of DOE does not constitute an endorsement by DOE of the views expressed in this article.

Appendix A: Fit Optimization and Error Analysis

The fitting of the model [Eq. (1)] to the experimental EXAFS spectrum is achieved by minimizing the X^2 (chi squared) function. To determine the uncertainty in the EXAFS fitting parameters R and σ^2 we use the inverse-Hessian method.[50] We actually vary two other parameters in the fitting, ΔE_0 and the amplitude multiplier S_0^2, but since we are mainly interested in the uncertainty in R and σ^2, we simplify the error calculation to the latter two parameters. The adjustment of S_0^2 and ΔE_0 is done by trial and error, and then the best values of R and σ^2 are determined by minimizing the two-dimensional X^2. We make use of the definition

$$X^2 = \sum_{j=1}^{N} \frac{\left[k\chi(\text{exp}) - k\chi(\text{theory})\right]^2}{N\delta^2}, \qquad \text{(A1)}$$

where δ is the mean root square of the noise in the data. The film data are digitized into a 2-D array of pixels s_{ij}. The signal is the average of m rows s_i in the direction of dispersion. As in Fig. 5 of Ref. 25, the noise is obtained by the average over the differences between adjacent pixel rows:

$$\sigma_{\text{noise}} = \sum_{i=1}^{m/2} \left(s_{2i-1} - s_{2i}\right)/m. \qquad \text{(A2)}$$

Here the random components of the measured signals add up, whereas the net signal cancels out. The two-dimensional matrix $X^2(R, \sigma^2)$ is used to find the best values of the parameters R and σ^2 as well as to derive the Hessian matrix $H_{ik} = \delta^2\chi^2/\delta a_i \delta a_k$, where $a_1 = R$ and $a_2 = \sigma^2$. The standard deviation in the parameters is obtained from C, the inverse matrix of H: $\Delta R = \left(C_{11}\right)^{1/2}$ and $\Delta\sigma^2 = \left(C_{22}\right)^{1/2}$. For the unshocked case (Fig. 94.45) we find ΔR = ±0.013 Å or a relative error of ~0.5% and $\Delta\sigma^2$ = ±0.002 Å^2 or a relative error of ~20%. This is in line with reported uncertainties in synchrotron experiments. The actual uncertainty in R can be higher because of imprecision in the x-ray wavelength scale, which is ~1%. This is of no concern here, however, because the interest is in shock-induced changes in R, which are of the order of ~10%.

To illustrate the error-calculation results we show in Fig. 94.49 the variation of X^2 with R for the optimal value of σ^2 and with σ^2 for the optimal value of R. The minimum value of X^2 is close to 1, which indicates that the errors in the experimental points are random. The vertical lines show the brackets of uncertainty derived from the two-dimensional Hessian analysis. For shocked-Ti experiments the uncertainties are higher: R = 2.66±0.05 Å or a relative error of ~2% and σ^2 = 0.033±0.008 Å^2 or a relative error of ~25%. The poor fit in Fig. 94.47 (mainly in R) indicates the inadequacy of Eq. (1) for the shocked result. Because of the large disorder contribution σ_{stat} (due possibly to a phase transition in Ti), a detailed EXAFS calculation relevant to the crystallographic structure of shocked Ti should be carried out.

REFERENCES

1. D. H. Kalantar *et al.*, Phys. Plasmas **7**, 1999 (2000).
2. L. Loveridge-Smith, A. Allen, J. Belak, T. Boehly, A. Hauer, B. Holian, D. Kalantar, G. Kyrala, R. W. Lee, P. Lomdahl, M. A. Meyers, D. Paisley, S. Pollaine, B. Remington, D. C. Swift, S. Weber, and J. S. Wark, Phys. Rev. Lett. **86**, 2349 (2001).
3. P. A. Lee *et al.*, Rev. Mod. Phys. **53**, 769 (1981).
4. K. Sakurai *et al.*, Appl. Phys. Lett. **57**, 2660 (1990).
5. M. L. Fdez–Gubieda *et al.*, Phys. Rev. B **53**, 620 (1996).
6. M. C. Ridgway *et al.*, Nucl. Instrum. Methods Phys. Res. B **147**, 148 (1999).
7. E. D. Crozier and A. J. Seary, Can. J. Phys. **58**, 1388 (1980); E. D. Crozier, in *EXAFS Spectroscopy: Techniques and Applications*, edited by B. K. Teo and D. C. Joy (Plenum Press, New York, 1981), Chap. 6, pp. 89–101.
8. G. Aquilanti *et al.*, J. Synchrotron Rad. **6**, 251 (1999).
9. Y. Katayama, O. Shimomura, and K. Tsuji, J. Non-Cryst. Solids **250–252**, 537 (1999).
10. R. B. Greegor and F. W. Lytle, Phys. Rev. B **20**, 4902 (1979).
11. K. Tamura *et al.*, J. Non-Cryst. Solids **150**, 351 (1992).
12. Y. Nishihata *et al.*, J. Phys., Condens. Matter **6**, 9317 (1994).

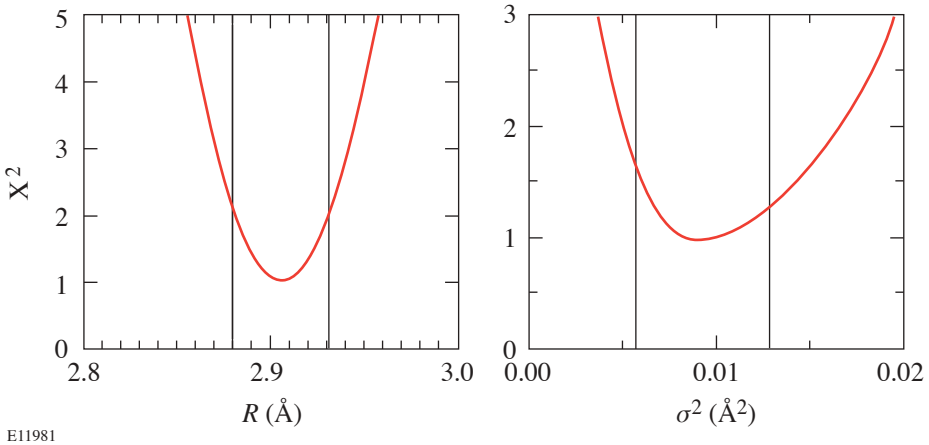

Figure 94.49
EXAFS spectrum fitting for the unshocked case (Fig. 94.43): the variation of X^2 with R for the optimal value of σ^2 and with σ^2 for the optimal value of R. The vertical lines show the standard deviation obtained from an inverse-Hessian analysis of X^2.

13. G. Dalba and P. Fornasini, J. Synchrotron Radiat. **4**, 243 (1997).
14. Y. Soldo *et al*., Phys. Rev. B **57**, 258 (1998).
15. A. Yoshiasa *et al*., J. Synchrotron Rad. **6**, 43 (1999).
16. L. Comez *et al*., Phys. Rev. B **65**, 014114 (2002).
17. A. Trapananti, A. Di Cicco, and M. Minicucci, Phys. Rev. B **66**, 014202 (2002).
18. R. C. Albers, A. K. McMahan, and J. E. Müller, Phys. Rev. B **31**, 3435 (1985).
19. A. Sadoc, J. P. Itie, and A. Polian, Philos. Mag. A, Phys. Condens. Matter Struct. Defects Mech. Prop. **80**, 2057 (2000).
20. P. A. Rigg and Y. M. Gupta, Phys. Rev. B **63**, 094112 (2001).
21. A. Hopkins and N. S. Brar, in *Shock Compression of Condensed Matter – 1999, AIP Conference Proceedings 505*, edited by M. D. Furnish, L. C. Chhabildas, and R. S. Hixson (American Institute of Physics, New York, 2000), pp. 423–426.
22. R. W. Eason *et al*., J. Phys. C, Solid State Phys. **17**, 5067 (1984).
23. B. A. Shiwai *et al*., Laser Part. Beams **10**, 41 (1992).
24. B. Yaakobi, F. J. Marshall, D. K. Bradley, J. A. Delettrez, R. S. Craxton, and R. Epstein, Phys. Plasmas **4**, 3021 (1997).
25. B. Yaakobi, F. J. Marshall, T. R. Boehly, R. P. J. Town, and D. D. Meyerhofer, J. Opt. Soc. Am. B **20**, 238 (2003).
26. T. R. Boehly, R. S. Craxton, T. H. Hinterman, J. H. Kelly, T. J. Kessler, S. A. Kumpan, S. A. Letzring, R. L. McCrory, S. F. B. Morse, W. Seka, S. Skupsky, J. M. Soures, and C. P. Verdon, Rev. Sci. Instrum. **66**, 508 (1995).
27. G. Blanche *et al*., Ultramicroscopy **50**, 141 (1993).
28. A. Balzarotti, M. De Crescenzi, and L. Incoccia, Phys. Rev. B **25**, 6349 (1982).
29. D. A. Young, *Phase Diagrams of the Elements* (University of California Press, Berkeley, CA, 1991).
30. C. W. Greeff, D. R. Trinkle, and R. C. Albers, J. Appl. Phys. **90**, 2221 (2001).
31. R. G. McQueen *et al*., in *High-Velocity Impact Phenomena*, edited by R. Kinslow (Academic Press, New York, 1970), Chap. VII, pp. 293–417.
32. H. Xia *et al*., Phys. Rev. B **42**, 6737 (1990).
33. Y. K. Vohra and P. T. Spencer, Phys. Rev. Lett. **86**, 3068 (2001).
34. A. K. Singh, M. Mohan, and C. Divakar, J. Appl. Phys. **53**, 1221 (1982).
35. H. Dammak, A. Dunlop, and D. Lesueur, Philos. Mag. A, Phys. Condens. Matter Struct. Defects Mech. Prop. **79**, 147 (1999).
36. B.-K. Teo and P. A. Lee, J. Am. Chem. Soc. **101**, 2815 (1979).
37. A. G. McKale *et al*., J. Am. Chem. Soc. **110**, 3763 (1988).
38. G. Beni and P. M. Platzman, Phys. Rev. B **14**, 1514 (1976).
39. R. M. More *et al*., Phys. Fluids **31**, 3059 (1988).
40. P. A. Lee and J. B. Pendry, Phys. Rev. B **11**, 2795 (1975).
41. J. Mustre de Leon *et al*., Phys. Rev. B **44**, 4146 (1991).
42. J. J. Rehr and R. C. Albers, Rev. Mod. Phys. **72**, 621 (2000).
43. E. A. Stern, B. A. Bunker, and S. M. Heald, Phys. Rev. B **21**, 5521 (1980).
44. B. L. Henke *et al*., J. Opt. Soc. Am. B **3**, 1540 (1986).
45. G. B. Zimmerman and W. L. Kruer, Comments Plasma Phys. Control. Fusion **2**, 51 (1975).
46. P. M. Celliers *et al*., Appl. Phys. Lett. **73**, 1320 (1998).
47. R. F. Trunin, G. V. Simakov, and A. B. Medvedev, Teplofiz. Vys. Temp. **37**, 881 (1999).
48. N. Dimakis and G. Bunker, Phys. Rev. B **58**, 2467 (1998).
49. J. A. Moriarty, D. A. Young, and M. Ross, Phys. Rev. B **30**, 578 (1984).
50. W. H. Press *et al*., *Numerical Recipes: The Art of Scientific Computing* (Cambridge University Press, Cambridge, England, 1987), Chap. 14, pp. 498–546.